



Article

# Enhanced Performance of Gold Nanoparticle-Modified Nickel-Iron Coatings for Sodium Borohydride Electrooxidation

Huma Amber <sup>1</sup>, Aušrinė Zabielaitė <sup>1</sup>, Aldona Balčiūnaitė <sup>1</sup>, Antanas Nacys <sup>1</sup>, Dmytro Shyshkin <sup>1,2</sup>, Birutė Šimkūnaitė-Stanynienė <sup>1</sup>, Zenius Mockus <sup>1</sup>, Jūratė Vaičiūnienė <sup>1</sup>, Loreta Tamašauskaitė-Tamašiūnaitė <sup>1,\*</sup> and Eugenijus Norkus <sup>1,\*</sup>

- <sup>1</sup> Center for Physical Sciences and Technology (FTMC), Saulėtekio Ave. 3, LT-10257 Vilnius, Lithuania; huma.amber@ftmc.lt (H.A.); ausrine.zabielaite@ftmc.lt (A.Z.); aldona.balciunaite@ftmc.lt (A.B.); antanas.nacys@ftmc.lt (A.N.); dmytro.shyshkin@chgf.stud.vu.lt (D.S.); birute.simkunaite@ftmc.lt (B.Š.-S.); zenius.mockus@ftmc.lt (Z.M.); jurate.vaiciuniene@ftmc.lt (J.V.)
- <sup>2</sup> Faculty of Chemistry and Geosciences, Vilnius University, Naugarduko Str. 24, LT-03225 Vilnius, Lithuania
- \* Correspondence: loreta.tamasauskaite@ftmc.lt (L.T.-T.); eugenijus.norkus@ftmc.lt (E.N.)

#### **Abstract**

The Ni-Fe coatings modified with AuNPs were deposited on the flexible copper-coated polyimide (Cu/PI) surface using electroless metal plating, while the galvanic displacement technique was applied to modify the surface of NiFe coatings by a small content of AuNPs in the range of 16.5  $\mu$ g<sub>Au</sub> cm<sup>-2</sup>. AuNPs of a few nanometers in size were deposited on the NiFe/Cu/PI surface by immersing it in a solution containing AuCl<sub>4</sub> ions. The electrooxidation of sodium borohydride was evaluated in a 1 M NaOH solution containing 0.05 M of sodium borohydride using cyclic voltammetry, chronoamperometry, and chronopotentiometry. In addition, the performance and stability of the NiFe/Cu/PI and AuNPs-NiFe/Cu/PI catalysts were evaluated for potential use in a direct NaBH<sub>4</sub>-H<sub>2</sub>O<sub>2</sub> fuel cell. The NiFe coating modified with AuNPs demonstrated significantly higher electrocatalytic activity towards the oxidation of sodium borohydride as compared to bare Au or unmodified NiFe/Cu/PI. Furthermore, it exhibited a superior power density of 89.7 mW cm<sup>-2</sup> at room temperature and operational stability under alkaline conditions, while the NiFe anode exhibited 73.1 mW cm<sup>-2</sup>. These results suggest that the AuNPsmodified NiFe coating has great potential as a material for use in direct borohydride fuel cells (DBFCs) applications involving the oxidation of sodium borohydride.

**Keywords:** gold nanoparticles; sodium borohydride; electrooxidation; electroless metal plating; galvanic displacement; fuel cells



Academic Editor: Fan Yang

Received: 22 August 2025 Revised: 12 September 2025 Accepted: 14 September 2025 Published: 19 September 2025

Citation: Amber, H.; Zabielaitė, A.; Balčiūnaitė, A.; Nacys, A.; Shyshkin, D.; Šimkūnaitė-Stanynienė, B.; Mockus, Z.; Vaičiūnienė, J.; Tamašauskaitė-Tamašiūnaitė, L.; Norkus, E. Enhanced Performance of Gold Nanoparticle-Modified Nickel-Iron Coatings for Sodium Borohydride Electrooxidation. *Crystals* 2025, 15, 819. https://doi.org/ 10.3390/cryst15090819

Copyright: © 2025 by the authors. Licensee MDPI, Basel, Switzerland. This article is an open access article distributed under the terms and conditions of the Creative Commons Attribution (CC BY) license (https://creativecommons.org/licenses/by/4.0/).

# 1. Introduction

Hydrogen has emerged as a potentially promising source of energy due to its clean and energy-efficient characteristics. It is regarded as a potential candidate for future implementation as an energy carrier [1]. Nevertheless, significant challenges persist in the domains of hydrogen storage and transport due to its low density and safety concerns [2]. Hydrogen-rich compounds, including sodium borohydride (NaBH<sub>4</sub>), which possesses a substantial hydrogen content of 10.6 wt% and an energy density of 9.3 Wh g $^{-1}$  [3], have emerged as a compelling candidate for carbon-free energy applications. This is attributable to its high energy density, environment-friendly profile, ease of handling in both liquid and solid phases, and abundant availability [4]. Due to these properties, NaBH<sub>4</sub> has been the focus of extensive research as a prospective fuel for DBFCs, which possess a high theoretical

cell voltage of 1.64 V [5,6]. The utilization of DBFCs in a wide range of applications is enabled by the aforementioned advantages. These applications include portable electronic devices, aerospace power systems, and other sectors that require short-term energy supply solutions [7]. DBFC functions through two fundamental half-cell reactions. The anodic half-reaction involves the borohydride oxidation reaction (BOR), while the cathodic half-reaction corresponds to the oxygen reduction reaction (ORR). The detailed electrochemical reactions are provided in the following Equations: (1)–(3) [8].

Anodic Reaction (BOR)—Oxidation of NaBH<sub>4</sub>:

$$BH_4^- + 8OH^- \to BO_2^- + 6H_2O + 8e^-$$
 E = -0.41 V vs. RHE (1)

Cathodic Reaction (ORR)—Oxygen Reduction Reaction:

$$2O_2 + 4H_2O + 8e^- \rightarrow 8OH^-$$
 E = 1.23 V vs. RHE (2)

Overall Cell Reaction:

$$BH_4^- + 2O_2 \rightarrow BO_2^- + 2H_2O$$
  $\Delta E = 1.64 V$  (3)

However, the BOR generally exhibits a high overpotential, which considerably restricts the output voltage of DBFCs. Therefore, it is imperative to rationally design BOR electrocatalysts to enhance their catalytic performance in order to optimize the overall efficiency of these fuel cells [9]. Conventional noble metal catalysts, including Pt [10], Ru [11], Pd [12], Au [13], and their alloys integrated with non-precious metals, such as PtCo/Co<sub>3</sub>O<sub>4</sub> nanosheets [14], Pd–Sn [15], Ni@Au [16], and Cu@Ag [17,18], have been extensively explored as electrocatalysts for the BOR. However, the high cost and limited abundance of noble metals pose substantial barriers to their large-scale application. It has been demonstrated that the BOR on gold (Au) proceeds via an eight-electron transfer mechanism, as Au functions as an efficient electrocatalyst for BOR rather than merely facilitating hydrolysis. However, the significantly high cost of Au poses a substantial obstacle to the commercialization of DBFC technology. Consequently, contemporary research endeavors are progressively concentrating on methodologies to reduce Au utilization in the formulation of anode catalysts, while preserving or amplifying their catalytic efficiency [19,20].

Given these circumstances, there is an urgent need to develop alternative, cost-effective electrocatalysts that demonstrate superior performance in the BOR. Recently, there has been an increasing focus on low-cost transition metals. These metals possess unfilled 3d orbitals, which favor the adsorption of BH<sub>4</sub><sup>-</sup> species. This property renders them promising candidates as primary components in BOR electrocatalyst design [21–23]. Threedimensional transition metals are distinguished by their inherent abundance, minimal cost, and advantageous theoretical catalytic properties. Among these elements, Fe [24], Co [25], Ni [26], and Zn [25,27] have been the focus of extensive research. The incorporation of these transition metals into noble metal-based catalysts has demonstrated effectiveness in two primary areas: the reduction in material costs and the enhancement of overall catalytic performance. Geng et al. investigated the potential of Ni–Pt/C as an anode catalyst for DBFCs, demonstrating its remarkable catalytic activity and stability for the BOR compared to Ni/C alone [28]. Duan et al. similarly reported that Cu-Pd/C bimetallic nanoparticles not only achieve catalytic performance comparable to that of Pd/C but also offer reduced material costs and enhanced electrocatalytic activity in alkaline media [29]. The findings indicate that the incorporation of 3d transition metals into noble metal-based catalysts can result in significant enhancements in catalytic performance.

Venugopal and colleagues conducted a comprehensive examination of the water–gas shift reaction, employing a series of catalysts composed of Au-M (M = Ag, Bi, Co, Cu, Mn, Ni, Pb, Ru, Sn, Tl) supported on  $Fe_2O_3$ . The study's results indicated that the catalytic activity of the Ni- and Ru-modified catalysts surpassed that of the unmodified  $Au/Fe_2O_3$  system. The enhanced performance of the Au–Ru system was predominantly attributable to the intrinsic activity of each metal, with minimal synergistic interaction. In contrast, the Au-Ni catalyst exhibited enhanced activity, which was predominantly attributed to synergistic effects between Au and Ni, as well as between Au and the  $Fe_2O_3$  support. Electronic (chemical) interactions contributed to this effect, to a certain extent [30]. Motivated by these observations, the objective of this study is to design, synthesize, and evaluate the activity of gold nanoparticles (AuNPs)-decorated NiFe coating on a flexible copper-coated polyimide (Cu/PI) surface for BOR. The electrocatalytic performance of the AuNPs-decorated NiFe coating for the BOR was comprehensively assessed in an alkaline medium using cyclic voltammetry (CV), chronoamperometry (CA), and chronopotentiometry (CP).

#### 2. Materials and Methods

## 2.1. Chemicals

Polyimide (PI) film of 0.125 mm thickness (DuPont<sup>TM</sup> Kapton<sup>®</sup> HN, GoodFellow), cobalt sulfate (CoSO<sub>4</sub>·7H<sub>2</sub>O, 98%, Chempur, Piekary Śląskie, Poland), sodium sulfide (Na<sub>2</sub>S·9H<sub>2</sub>O, 99.99%, Sigma-Aldrich, Taufkirchen, Germany), palladium chloride (PdCl<sub>2</sub>, 59.5%, Alfa Aesar, Ward Hill, MA, USA), copper sulfate pentahydrate (CuSO<sub>4</sub>·5H<sub>2</sub>O, 98%, Chempur, Piekary Śląskie, Poland), iron sulfate heptahydrate (FeSO<sub>4</sub>·7H<sub>2</sub>O, 97%, Chempur, Piekary Śląskie, Poland), nickel sulfate (NiSO<sub>4</sub>·7H<sub>2</sub>O, >98%, Chempur, Piekary Śląskie, Poland), ethylenediaminetetraacetic acid (EDTA, 99%, Reachem, Mississauga, Canada), sodium malonate (CH<sub>2</sub>(COONa)<sub>2</sub>, 97%, Merck, Darmstadt, Germany), morpholine borane (MB, C<sub>4</sub>H<sub>8</sub>ONH·BH<sub>3</sub>, 97%, Alfa Aesar, Ward Hill, MA, USA), sulfuric acid (H<sub>2</sub>SO<sub>4</sub>, 98%, Chempur, Piekary Śląskie, Poland), sodium hydroxide (99%, Chempur, Piekary Śląskie, Poland), sodium borohydride (NaBH<sub>4</sub>, 99%, Merck, Darmstadt, Germany).

## 2.2. Fabrication of NiFe and AuNPs-Modified NiFe

This study presents a simple, two-step approach for fabricating Au nanoparticle-modified NiFe catalysts. The first step involves electroless NiFe deposition on flexible, copper-coated polyimide (Cu/PI). The second step involves spontaneous Au displacement from the HAuCl<sub>4</sub> solution. The flexible substrate used is a polyimide (DuPont<sup>TM</sup> Kapton<sup>®</sup>, Goodfellow Cambridge Limited, Huntingdon, UK). PI is non-conductive, so its surface was pre-treated by using adhesion/activation pretreatment procedures as described in reference [31]. A thin, conductive CoS layer was formed on the PI surface using the SILAR method. Then, a Cu layer was electrodeposited on the CoS/PI surface. Finally, the NiFe coating was deposited on the Cu/PI using the following procedures:

- Activation of Cu/PI by dipping it in a 0.5 g L<sup>-1</sup> PdCl<sub>2</sub> solution for 1 min, followed by rinsing with deionized water.
- Electroless plating of the NiFe coating onto the activated Cu/PI with Pd by immersing it in an electroless plating solution containing 0.14 M NiSO<sub>4</sub>, 1 mM FeSO<sub>4</sub>, 0.05 M EDTA, 0.1 M CH<sub>2</sub>(COONa)<sub>2</sub>, 0.2 M MB, and 0.2 M NH<sub>2</sub>CH<sub>2</sub>COOH (pH 7). The bath operated at 60 °C for 1 h.

The AuNPs were deposited on the prepared NiFe/Cu/PI electrode via the galvanic displacement technique [32]. The NiFe/Cu/PI electrode was immersed in 1 mM HAuCl $_4$  for 1 min, followed by rinsing with deionized water and drying. Figure 1 shows a general fabrication scheme of the catalysts.

Crystals 2025, 15, 819 4 of 16

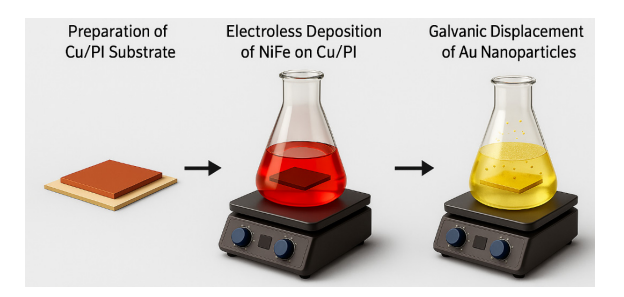


Figure 1. Fabrication scheme of the NiFe and AuNPs-NiFe catalysts.

### 2.3. Characterization of Materials

The surface morphology and elemental composition of the catalyst were evaluated using an SEM-focused ion beam facility (Helios Nanolab 650, FEI, Eindhoven, The Netherlands) equipped with an EDX spectrometer (INCA Energy 350 X-Max 20, Oxford Instruments, Oxford, UK).

The XRD patterns of the prepared materials were measured using a SmartLab X-ray diffractometer (Rigaku, Tokyo, Japan), which was equipped with a 9 kW rotating Cu anode X-ray tube. The grazing incidence (GIXRD) method was used in the  $2\theta$  range of 15– $90^{\circ}$ . The angle between the parallel X-ray beam and the specimen surface ( $\omega$  angle) was adjusted to  $0.5^{\circ}$ . Phase identification was performed using the PDXL software package (Rigaku) and the ICDD powder diffraction database PDF-4+ (2022 release).

The composition of the prepared catalysts was determined using an ICP optical emission spectrometer Optima700DV (Perkin Elmer, Waltham, MA, USA).

#### 2.4. Electrochemical Measurements

The BOR was investigated using a potentiostat/galvanostat PGSTAT100 (Metrohm Autolab B. V., Utrecht, The Netherlands). A conventional three-electrode cell was used for electrochemical measurements. The NiFe/Cu/PI and AuNPs-NiFe/Cu/PI catalysts with a geometric area of 2 cm² were employed as working electrodes. An  $Hg_2Cl_2$  (3.5 M KCl) electrode was used as a reference, Pt sheet with a geometric area of 4 cm² was used as a counter electrode. For comparison, the bare Au electrode with a geometric area of 0.636 cm² was used. Cyclic voltammograms (CVs) were recorded at a potential scan rate of 10 mV s $^{-1}$  from the open-circuit potential value in the anodic part up to +0.6 V unless otherwise stated in a 1 M NaOH solution containing NaBH<sub>4</sub> concentration of 0.05 M at a temperature of 25 °C. Chronoamperometry test was carried out at a constant potential value of -0.2 V for 10 h, while chronopotentiometry test was carried out at a constant current density of 10 mA cm $^{-2}$  versus the geometric area of the investigated catalysts for 10 h.

All reported potential values are referred to as "SCE".

## 2.5. Fuel Cell Test Experiments

Direct experiments were conducted on a NaBH $_4$ -H $_2$ O $_2$  fuel cell employing NiFe and AuNPs-NiFe catalysts, with an anode with a geometric area of 1 cm $^2$ . A Pt sheet was used as the cathode. These were placed on either side of the middle container. The anodic and cathodic compartments of the fuel cells were separated by means of a Nafion N117 membrane. The anolyte utilized was an alkaline mixture of 1 M NaBH $_4$  and 4 M NaOH, while the catholyte was a solution of 1.5 M HCl and 5 M H $_2$ O $_2$ . Each cell compartment was filled with 100 mL of freshly prepared electrolyte. The current densities presented were then normalized with respect to the geometric area of the catalysts. Electrochemical measurements were assessed using a Zennium workstation (ZAHNER-Elektrik GmbH

Crystals **2025**, 15, 819 5 of 16

& Co. KG, Kronach, Germany). Cell polarization curves were recorded at temperatures ranging from 25 to 55  $^{\circ}$ C.

# 3. Results and Discussion

In this study we present a strategy to fabricate flexible electrocatalysts based on Ni-Fe coatings modified with AuNPs. As flexible substrate we use polyimide which is lightweight, flexible, resistant to heat and chemicals. MB was chosen as a reducing agent for depositing the NiFe coating because it is a relatively mild, stable, less explosive and toxic, and environmentally friendly alternative to traditional reducing agents like hydrazine ( $N_2H_4$ ) or NaBH4. In addition, MB is also stable in solution, which allows for a longer plating bath life. Figure 2a–c present SEM views of the NiFe coating at different magnifications. The surface exhibits a cauliflower-like morphology, with individual grains or clusters that appear tightly packed together. The grains are irregularly shaped and separated by grain boundaries. The coating is dense and continuous, indicating good substrate coverage.

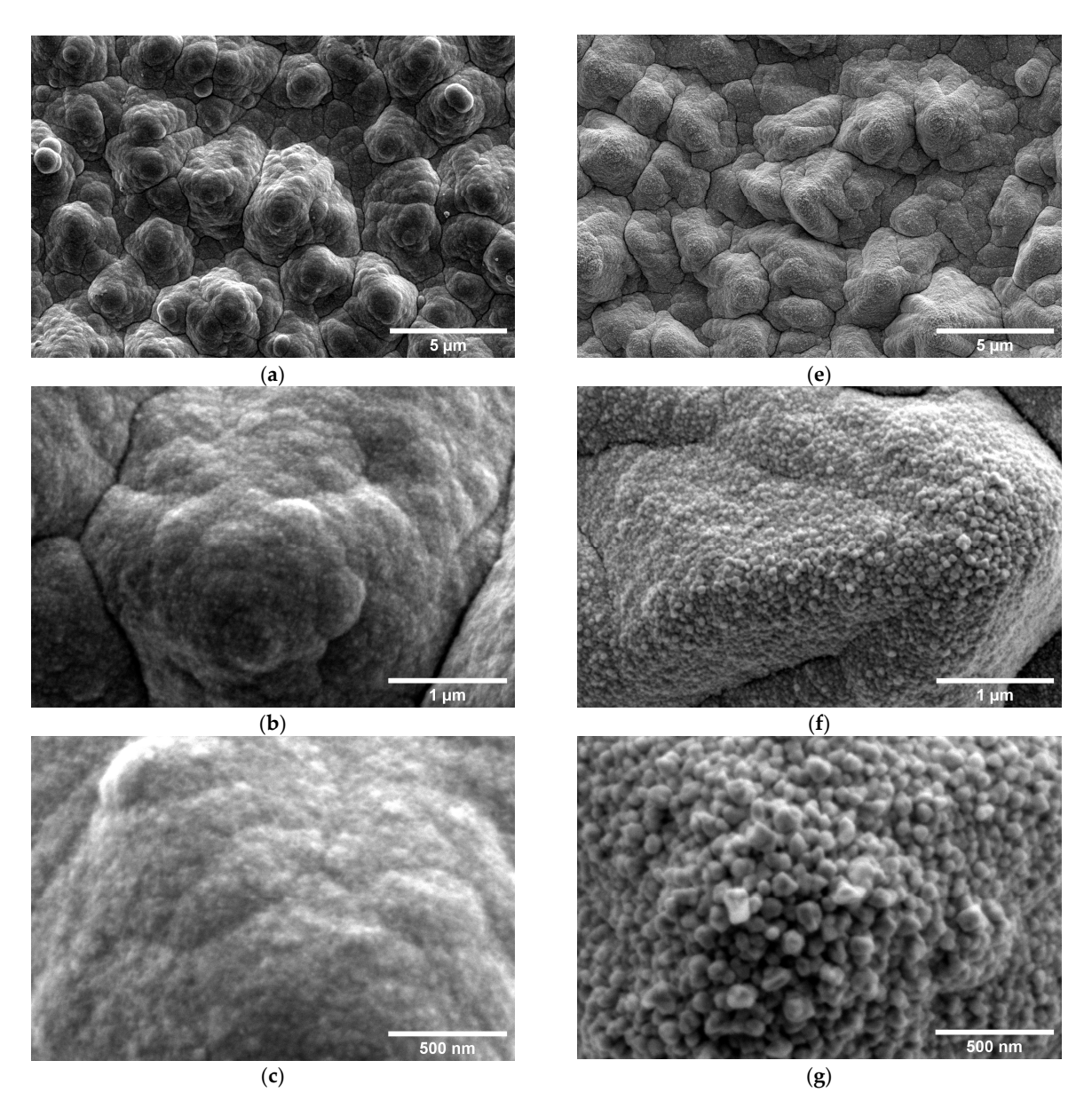
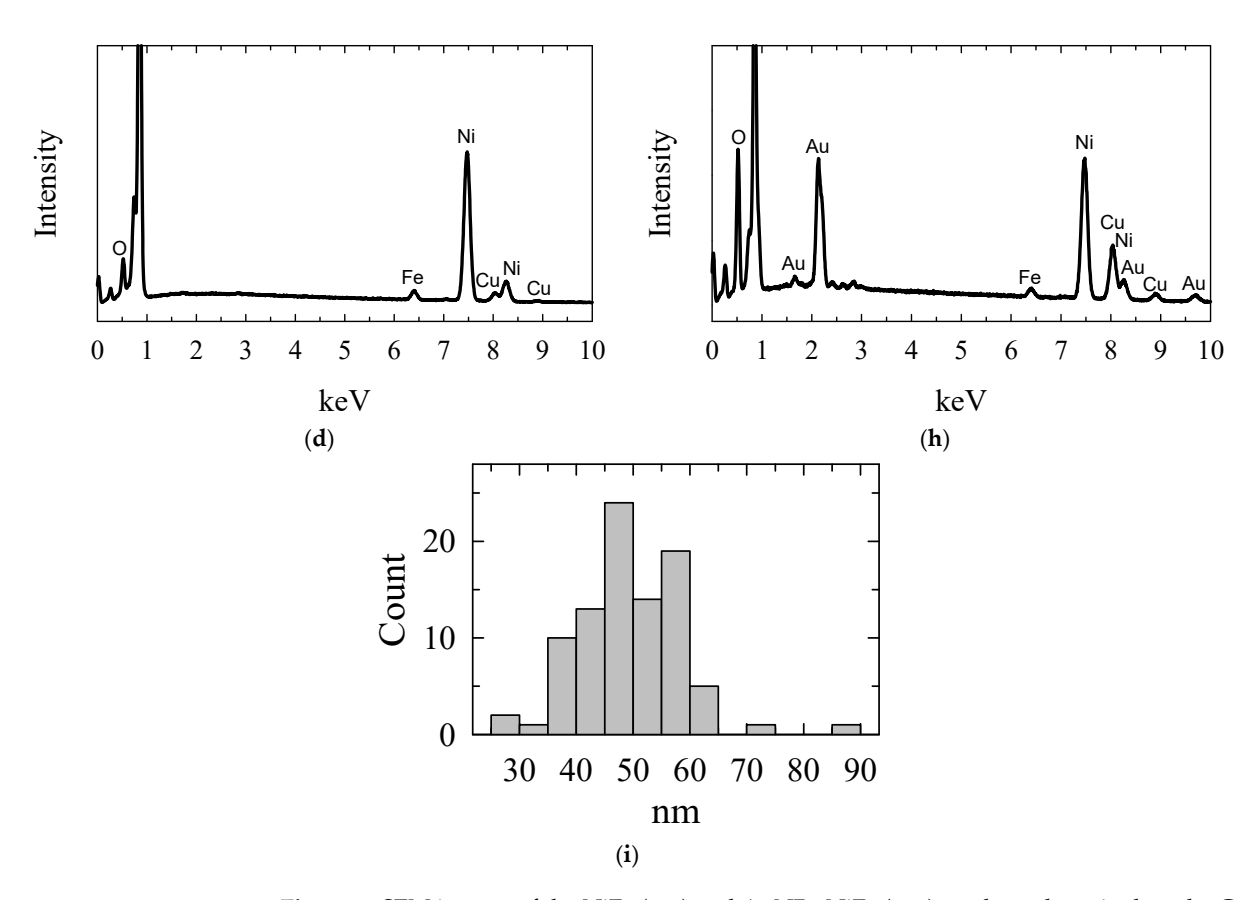


Figure 2. Cont.

Crystals **2025**, 15, 819 6 of 16



**Figure 2.** SEM images of the NiFe (**a**–**c**) and AuNPs-NiFe (**e**–**g**) catalysts deposited on the Cu/PI surface. (**d**,**h**) The corresponding EDX spectra. (**i**) Particle distribution histogram of AuNPs-NiFe/Cu/PI.

AuNPs were deposited on the NiFe coating by immersing it in a gold-containing solution for 1 min. This simple procedure is known as galvanic displacement, whereby a noble metal is deposited through the oxidation of a precursor metal adlayer deposited on the substrate at open-circuit potential [32]. SEM images of the prepared AuNPs-modified NiFe coating at different magnifications are shown in Figure 2e–g. As with the previous images (Figure 2a–c), the structure retains a cauliflower-like morphology, indicating that the deposition of AuNPs did not damage the base layer. The modification of the NiFe coating by Au via galvanic displacement occurs by deposition of small Au nanoparticles with diameters ranging from 40 to 60 nm (Figure 2i), which are close one to other and later coalesce or grow into a more continuous film. The individual grains or clusters appear rounded and densely packed, suggesting a uniform deposition process. Furthermore, the surface is highly structured, roughened, and nanoparticle-rich (Figure 2f,g).

Figure 2d,h show the energy dispersive X-ray (EDX) spectra corresponding to the NiFe and AuNPs-NiFe catalysts, respectively. These spectra confirm the presence of Ni, Fe and Au in both catalytic materials. The composition of the deposited NiFe and AuNPs-NiFe catalysts was determined using inductively coupled plasma optical emission spectroscopy (ICP-OES). The summarized data are given in Table 1.

**Table 1.** The data of the composition of the prepared catalysts by ICP-OES analysis.

Catalyst –		Element, at%	
	Au	Ni	Fe
NiFe	-	96	4
AuNPs-NiFe	5	93	2

Crystals **2025**, 15, 819 7 of 16

The results showed that the NiFe coating deposited on Cu/PI contained approximately 96 at% of Ni and 4 at% of Fe, while the AuNPs-NiFe catalyst contained 93 at% of Ni, 2 at% of Fe, and 5 at% of Au. Additionally, the Au loading was approximately  $16.5 \,\mu g \, cm^{-2}$ .

X-ray diffraction was used to evaluate the crystal structure of the materials under investigation. Figure 3a shows the XRD patterns for NiFe/Cu/PI. The peaks at  $2\theta$  values of  $43.29^{\circ}$ ,  $50.43^{\circ}$ ,  $74.13^{\circ}$ ,  $89.92^{\circ}$ , and  $95.17^{\circ}$  correspond to the (111), (200), (220), (311), and (222) planes, respectively, and confirm the cubic lattice of Cu. All the XRD peaks are in good agreement with the standard pattern for pure face-centered cubic planes of Cu (PDF card no. 00-004-0836).

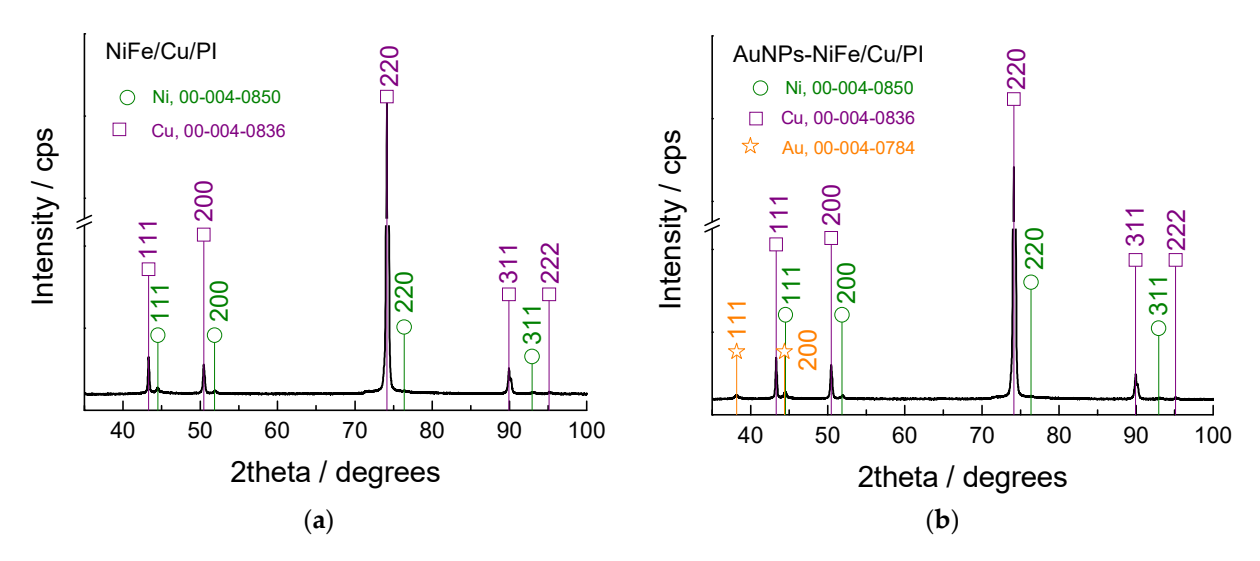


**Figure 3.** XRD patterns of NiFe/Cu/PI (a) and AuNPs-NiFe/Cu/PI (b). Peaks positions are indicated according to database PDF4+ data card: Ni—card. no. 00-004-0850, Cu—card. no. 00-004-0836, and Au—card. no. 00-004-0784.

The XRD peaks at 20 values of  $44.42^{\circ}$ ,  $51.94^{\circ}$ ,  $76.37^{\circ}$ , and  $92.97^{\circ}$ , correspond to the (111), (200), (220), and (311) planes, respectively. These are attributed to the cubic lattice of Ni, according to the pure face-centered cubic plane of Ni (PDF card. no. 00-004-0850). Furthermore, the peaks at approximately  $43.29^{\circ}$ ,  $50.43^{\circ}$ , and  $74.13^{\circ}$  overlap with the Cu XRD peaks and can be indexed to the (111), (200), and (220) planes of the fcc Fe-Ni alloy (JCPDS card no. 47-1405) [33]. In the case of AuNPs-NiFe, the additional XRD peaks at 20 values of  $38.12^{\circ}$  and  $44.45^{\circ}$  can be indexed to the (111) and (200) planes of fcc Au (PDF card no. 00-004-0784) (see Figure 3b).

The electrocatalytic properties of bare Au, NiFe, and AuNPs-modified NiFe coatings towards sodium borohydride oxidation were investigated using cyclic voltammetry. Figure 4 shows the oxidation of borohydride on a bare Au electrode (a), an unmodified NiFe electrode (b and c), and an AuNPs-modified NiFe electrode (d). The solid lines in Figure 4b,d represent the CVs recorded in a background solution containing 1 M NaOH. Figure 4e,f show bar columns of current densities and potential values, respectively, under peak A for the bare Au and AuNPs-NiFe catalysts.

In the case of the bare Au catalyst, a broad anodic peak A is evident at a potential of -0.36 V within the positive potential scan, as illustrated in Figure 4a. This oxidation peak has been attributed to the direct oxidation of  $BH_4^-$  ions, as depicted in Equation (1) [34]. Moreover, a broad oxidation wave extending up to 0.4 V is concomitant with the oxidation of reaction intermediates on the partially oxidized gold surface. In the reverse scan, a sharp peak B is observed at ca. 0.27 V (Figure 4a). The potential exhibited a peak at 0.27 V, followed by a plateau in the potential region from 0.0 to -0.6 V, which corresponds to the oxidation of adsorbed species such as  $BH_3OH^-$  or other borohydrides formed as

intermediates during the oxidation of  $BH_4^-$  ion in the forward scan [34]. However, the BOR current densities on the bare Au electrode decrease in subsequent scan cycles (Figure 4a). This can probably be due to the formation of intermediates adsorbed on the electrode in the electrocatalytic process, so the poisoned surface of the electrode diminished the electrocatalytic activity of the bare gold electrode [34].

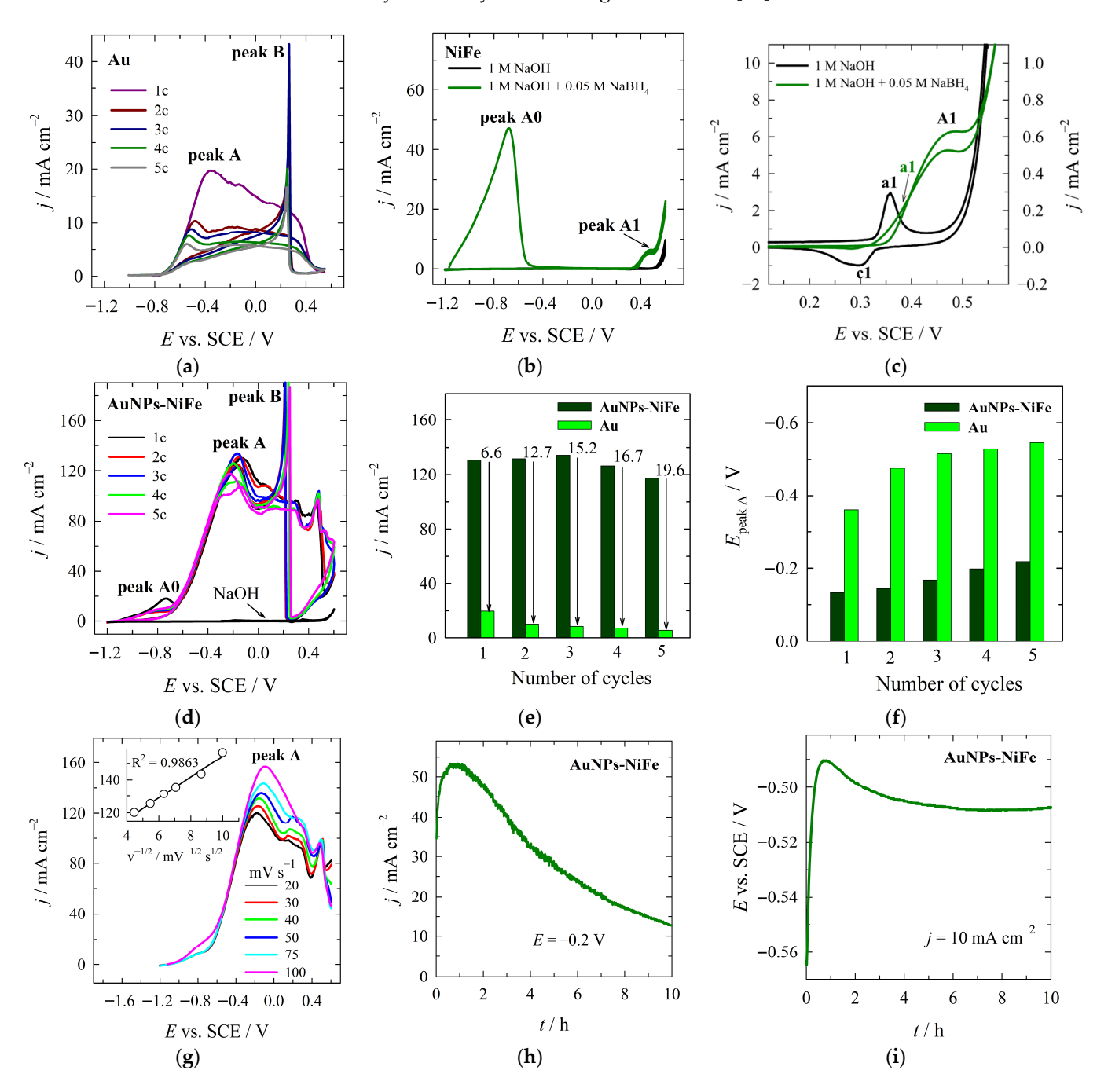


**Figure 4.** CVs of Au (a), NiFe (b,c), and AuNPs-NiFe (d) catalysts recorded in 0.05 M NaBH<sub>4</sub> + 1 M NaOH and 1 M NaOH (b-d) at 10 mV s<sup>-1</sup>. (c) presents the CVs for NiFe at lower potential window. Bar columns of current densities (e) and potential values (f) under peak A for the bare Au and AuNPs-NiFe catalysts. (g) LSVs of AuNPs-NiFe recorded in 0.05 M NaBH<sub>4</sub> + 1 M NaOH at different potential scan rates. (h) shows CA curve recorded on AuNPs-NiFe at a constant potential of -0.2 V for 10 h. (i) shows CP curve recorded at a current density of 10 mA cm<sup>-2</sup> for 10 h.

In the case of the NiFe catalyst, two oxidation peaks (A0 and A1) are visible in the cyclic voltammogram (Figure 4b). The first peak, which occurs at low overpotentials, may be

related to the oxidation of hydrogen generated by sodium borohydride hydrolysis [34,35], while the second peak A1, which occurs at potentials greater than 0.4 V, may be related to the direct oxidation of sodium borohydride. Figure 4c shows similar CVs to those presented in Figure 4b, but in the lower potential region. The black line presents the CV of NiFe recorded in a 1 M NaOH background solution, while the green line shows the CV recorded in a NaBH<sub>4</sub> solution at NiFe. During an anodic scan of NiFe in the background solution, an anodic peak (a1) at 0.36 V is observed. In the reverse scan, a cathodic peak (c1) is detected, which is assigned to the  $Ni^{2+}/Ni^{3+}$  redox process [36]. In the case of the CV of NiFe in a 1 M NaOH solution containing 0.05 M NaBH<sub>4</sub> (Figure 4c, green line), the peak a1 is hardly distinguishable, followed by the appearance of a peak A1 at a more positive potential value of 0.48 V vs. SCE are observed. The current density of the anodic peak A1 was so large that the anodic peak a became ill-defined (Figure 4c). It can therefore be concluded that the oxidation of NaBH<sub>4</sub> took place after the oxidation of Ni(OH)<sub>2</sub> to NiOOH [37–40]. The Ni<sup>2+</sup>/Ni<sup>3+</sup> redox couple acts as a catalyst for the oxidation of NaBH<sub>4</sub>. Moreover, no anodic peaks were observed at negative potential values during subsequent anodic scans on this catalyst, indicating that the surface of the NiFe catalyst is inactive and does not catalyze the direct oxidation of BH<sub>4</sub><sup>-</sup> ions at higher potentials. This is due to passivation caused by the formation of Ni(hydr)oxide(s) [39,41], or possibly the poisoning of the catalyst surface by strongly adsorbed intermediates generated during BH<sub>4</sub><sup>-</sup> ion oxidation [34].

In contrast, the BOR on the AuNPs-modified NiFe catalyst proceeds in the same manner as on the bare Au electrode (see Figure 4a,d). The BOR starts at an electrode potential value of approximately -0.70 V on the Au electrode and -0.66 V on the AuNPs-NiFe catalyst. This is followed by broad oxidation peaks A, which are related to direct borohydride oxidation and are observed at -0.36 V and -0.13 V, respectively. As can be seen in Figure 4a,d, the potential values of the first anodic peak A on the AuNPs-NiFe catalyst are shifted by 0.22 V towards positive potential values compared to the bare Au electrode (Figure 4e). During the long-term potential cycling for AuNPs-NiFe between ca. -1.2 and +0.6 V for 5 cycles (Figure 4d), between -1.0 and +0.5 V for Au electrode (Figure 4a), and between ca. -1.2 and +0.6 V for NiFe (Figure 4b), the significantly higher BOR currents were obtained on the AuNPs-modified NiFe coating compared to the bare Au and unmodified NiFe electrodes, exhibiting increased catalytic properties of this catalyst. Therefore, sharp peaks B in the negative scan at the AuNPs-NiFe catalyst are observed at ca. +0.20 V (Figure 4d). Furthermore, the BOR current densities recorded on the AuNPs modified NiFe exhibits ca. 6.6 (first cycle) and 19.6 (fifth cycle) times higher current densities compared with those at the bare Au electrode (Figure 4e). Furthermore, during the long-term potential scanning, the potential values of peak A shift towards more negative potential values for the bare Au and AuNPs-NiFe catalysts, indicating the high activity of the AuNPs-NiFe and Au electrodes (Figure 4f). The deposition of a small amount of AuNPs significantly enhances the activity of the NiFe catalyst for the BOR. The enhanced oxidation currents of the AuNPs-NiFe catalyst can be attributed to the electrocatalytic properties of gold and metal particles, and gold-metal alloy formation [42,43]. Modification by AuNPs is implicated in higher catalytic activity due to providing active sites or improving charge transfer. Additionally, the AuNPs can improve the chemical stability of the coating and, therefore, increase electrical conductivity.

Figure 4g shows LSVs recorded on the AuNPs-NiFe catalyst in  $0.05\,M$  NaBH $_4+1\,M$  NaOH solution at different scan rates. As can be seen, the current density of peak A increases with an increase in the scan rate, indicating that the BOR is diffusion-controlled.

The chronoamperometric response of the AuNPs-NiFe catalyst was investigated in a  $0.05 \,\mathrm{M\,NaBH_4} + 1 \,\mathrm{M\,NaOH}$  solution at a constant potential of  $-0.2 \,\mathrm{V}$  for 10 h (see Figure 4h). After 1 h, the current density of the AuNPs-NiFe catalyst was ca. 52 mA cm<sup>-2</sup>, followed by

decay characteristic of diffusion limited systems. Furthermore, the decay in current may be related to poisoning of the catalyst surface by adsorption of BOR intermediates (e.g.,  $BH_3OH^-$ ,  $B(OH)_3$ ). According to the CA measurements, the stability of the AuNPs-NiFe catalyst is insufficient and must be improved. The catalyst surface can be recovered from poisoning by sodium borohydride oxidation products using post-treatment cleaning (e.g., with NaBH<sub>4</sub>) or electrochemical potential-step cleaning [44]. Furthermore, enhancing the long-term stability of the AuNPs-NiFe catalyst can be achieved by incorporating dopants or optimizing the electrode design.

Figure 4i presents the chronopotentiometric response of the AuNPs-NiFe catalyst at a constant current density of  $10~\text{mA}~\text{cm}^{-2}$ . The difference between the steady-state operating anode potential after 10~h and the open-circuit potential was very small, indicating good electroactivity. Table 2 shows a comparison of the peak current densities during the oxidation of NaBH<sub>4</sub> on the NiFe/Cu/PI and AuNPs-NiFe/Cu/PI catalysts, as well as on other catalytic materials reported in the literature. AuNPs-NiFe/Cu/PI exhibits higher electrocatalytic activity for the oxidation of NaBH<sub>4</sub> than the other catalytic materials, such as leached Ni/Zn-Ni (125.8 mA cm $^{-2}$ ) [36], nanoporous gold wire array (73.6 mA cm $^{-2}$ ) [45], Au<sub>2</sub>Ni<sub>1</sub>Cu<sub>1</sub>/C (61.4 mA cm $^{-2}$ ) [46], and Ni deposited carbon fiber (56 mA cm $^{-2}$ ) and is promising DBFC anode material.

**Table 2.** Comparison of the peak current density during NaBH<sub>4</sub> oxidation on NiFe/Cu/PI and AuNPs-NiFe/Cu/PI catalysts and different catalytic materials.

Sample	Electrolyte	Scan Rate, mV $\rm s^{-1}$	Peak Current Density, mA cm <sup>-2</sup>	Ref.
NiFe/Cu/PI	0.05 M NaBH <sub>4</sub> + 1 M NaOH	10	6.3	This study
AuNPs-NiFe/Cu/PI	$0.05 \text{ M NaBH}_4 + 1 \text{ M NaOH}$	10	133.9	This study
Ni deposited carbon fiber	$0.8 \text{ M NaBH}_4 + 2 \text{ M NaOH}$	50	56.0	[38]
Ni/C	$0.2 \text{ M NaBH}_4 + 2 \text{ M NaOH}$	50	18.0	[28]
Leached Ni/Zn-Ni	$0.02 \text{ M NaBH}_4 + 1 \text{ M NaOH}$	10	125.8	[36]
Nanoporous gold wire array	$0.02 \text{ M NaBH}_4 + 1 \text{ M NaOH}$	10	73.6	[45]
Ni <sub>1</sub> @Au <sub>1</sub> /C	0.03 M NaBH <sub>4</sub> + 1 M NaOH	50	26.0	[16]
$Au_2Ni_1Cu_1/C$	$0.1 \text{ M NaBH}_4 + 2 \text{ M NaOH}$	50	61.4	[46]
Au-Y	0.03 M NaBH <sub>4</sub> + 2 M NaOH	50	34.0	[47]
$Au_{50}Fe_{50}/C$	$0.1 \text{ M NaBH}_4 + 3 \text{ M NaOH}$	20	33.8	[48]

The NiFe/Cu/PI and AuNPs-NiFe/Cu/PI catalysts have been investigated for use as anode catalysts in sodium borohydride–hydrogen peroxide fuel cells (DBHPFCs, NaBH<sub>4</sub>- $\rm H_2O_2$ ). DBHPFCs operate through the oxidation of BH<sub>4</sub><sup>-</sup> at the anode (Equation (1)) and the reduction of hydrogen peroxide at the cathode (Equation (4)):

$$4HO_2^- + 4H_2O + 8e^- \rightarrow 12OH^ E_{oc} = 0.87 \text{ V vs. SHE}$$
 (4)

The overall reaction is as follows:

$$4HO_2^- + BH_4^- \rightarrow 4OH^- + BO_2 + 2H_2O$$
  $E_{ocell} = 2.11 \text{ V vs. SHE}$  (5)

The performance of the DBHPFC was evaluated by recording the cell polarization and obtaining the corresponding power density curves at different temperatures. Figure 5 presents the cell polarization and peak power density curves recorded at different temperatures on NiFe (a) and NiFe modified with AuNPs (b) for NaBH<sub>4</sub>-H<sub>2</sub>O<sub>2</sub> fuel cell. A Pt sheet was used as the cathode. The fuel cells displayed an open circuit voltage of ca. 1.9 V when the NiFe and AuNPs-NiFe catalysts were employed as the anodes (see Figure 5). The summarized data are given in Table 3. The NiFe catalyst exhibited peak power density values of ca. 73.1–93.6 mW cm $^{-2}$  at temperatures of 25–55 °C, whereas the AuNPs-NiFe

catalyst with a Au loading of 16.5  $\mu g_{Au}$  cm<sup>-2</sup> achieved greater peak power density values of ca. 89.7–126.3 at temperatures of 25–55 °C.

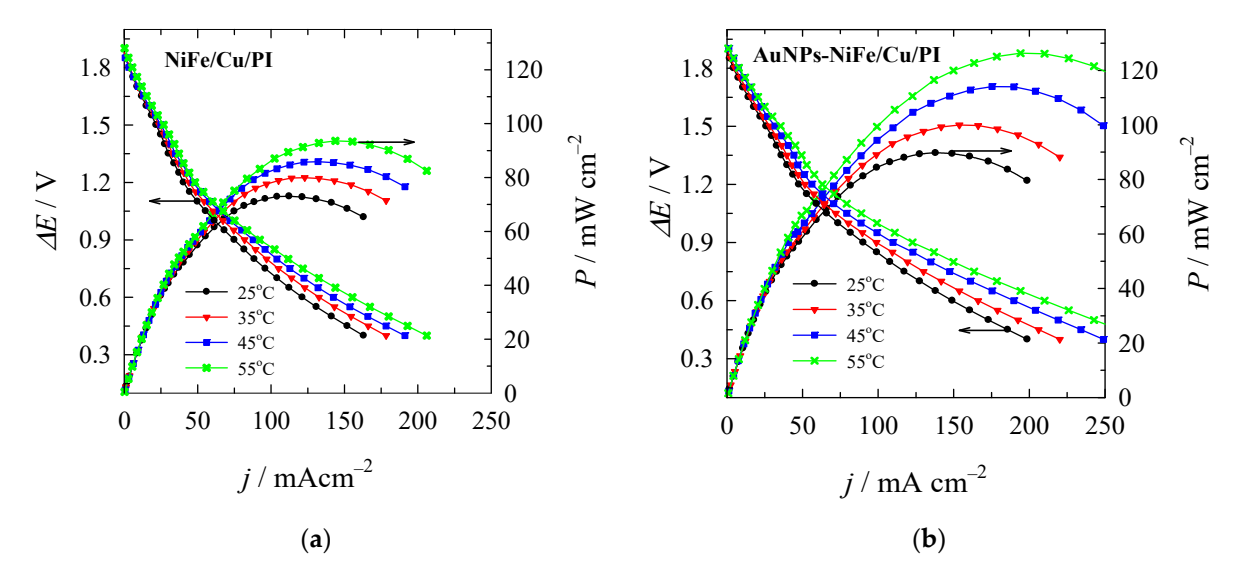


**Figure 5.** Cell polarization and power density curves for the direct NaBH<sub>4</sub>-H<sub>2</sub>O<sub>2</sub> fuel cell using NiFe/Cu/PI (a) and AuNPs-NiFe/Cu/PI (b) catalysts as the anodes/cathodes using the anolyte consisting of 1 M NaBH<sub>4</sub> and 4 M NaOH and the catholyte consisting of 5 M H<sub>2</sub>O<sub>2</sub> and 1.5 M HCl at different temperatures.

**Table 3.** Fuel cell parameters of NaBH<sub>4</sub>-H<sub>2</sub>O<sub>2</sub> employing NiFe/Cu/PI and AuNPs-NiFe/Cu/PI anode catalysts.

Sample	T, °C	Peak Power Density, mW cm <sup>-2</sup>	Peak Power Density, mW μg <sub>Au</sub> <sup>-1</sup>	Current Density at Peak Power Density, mA cm <sup>-2</sup>	Cell Voltage at Peak Power Density, V
NiFe/Cu/PI	25	73.1	4.4	112.3	0.65
	35	80.0	4.8	122.9	0.65
	45	85.9	5.2	132.0	0.65
	55	93.6	5.7	143.9	0.65
AuNPs-NiFe/Cu/PI	25	89.7	5.4	137.9	0.65
	35	100.0	6.1	153.7	0.65
	45	114.1	6.9	175.4	0.65
	55	126.3	7.6	194.2	0.65

The AuNPs-modified NiFe anode exhibited superior power density (89.7 mW cm $^{-2}$ ) at room temperature and operational stability under alkaline conditions, whereas the unmodified NiFe anode exhibited 73.1 mW cm $^{-2}$ . Specific peak power density values in the range of 5.4–7.6 mW  $\mu g_{Au}^{-1}$  at 25–55 °C were obtained using the AuNPs-modified NiFe catalyst (Table 3). The comparison of DBPFC performance using different anode electrocatalysts is shown in Table 4.

**Table 4.** The comparison of DBPFC performance using different anode electrocatalysts.

Anode	Cathode	Anolyte	Catholyte	$P_{max}$ , mW cm <sup>-2</sup>	T, °C	Ref.
NiFe/Cu/PI	Pt	$0.05\mathrm{M}\mathrm{NaBH_4} + 1\mathrm{M}\mathrm{NaOH}$	$5 \mathrm{M}\mathrm{H}_2\mathrm{O}_2 + 1.5 \mathrm{M}\mathrm{HCl}$	73.1 93.6	25 55	[This work]
AuNPs- NiFe/Cu/PI	Pt	$0.05\mathrm{M}\mathrm{NaBH_4} + 1\mathrm{M}\mathrm{NaOH}$	$5 \mathrm{M}\mathrm{H}_2\mathrm{O}_2 + 1.5 \mathrm{M}\mathrm{HCl}$	89.7 126.3	25 55	[This work]
Ni <sub>1</sub> @Au <sub>2</sub> /C	Pt mesh	$2\mathrm{M}\mathrm{NaOH}$ + $0.5\mathrm{M}\mathrm{NaBH}_4$	4.5 M H <sub>2</sub> O <sub>2</sub> + 2 M HCl	74	20	[16]
Cu <sub>1</sub> Pd <sub>1</sub> /C	Pt mesh	0.5 M NaBH <sub>4</sub> + 2 M NaOH	4.5 M H <sub>2</sub> O <sub>2</sub> + 2 M HCl	39.82	20	[29]

Crystals 2025, 15, 819 12 of 16

Table 4. Cont.

Anode	Cathode	Anolyte	Catholyte	P <sub>max</sub> , mW cm <sup>-2</sup>	T, °C	Ref.
Au <sub>50</sub> Fe <sub>50</sub> /C	Au/C	$0.1\mathrm{M}\mathrm{NaBH_4} + 3\mathrm{M}\mathrm{NaOH}$	$2 \text{ M H}_2\text{O}_2 + 0.5 \text{ M H}_2\text{SO}_4$	34.9	25	[46]
Au <sub>58</sub> Ni <sub>42</sub> /C	Au/C	$1 \mathrm{M}\mathrm{NaBH_4} + 3 \mathrm{M}\mathrm{NaOH}$	$2 \text{ M H}_2\text{O}_2 + 0.5 \text{ M H}_2\text{SO}_4$	45.74	20	[49]
HNAu/C	SNAu/C	1 M NaBH <sub>4</sub> + 3 M NaOH	2 M H <sub>2</sub> O <sub>2</sub> + 0.5 M H <sub>2</sub> SO <sub>4</sub>	25.8	20	[50]
Au@Co-B	LaCoO <sub>3</sub>	0.8 M KBH <sub>4</sub> + 6 M NaOH	Air	85	25	[51]
Au0 <sub>75</sub> Cu <sub>25</sub> /C	Au/C	3 M NaOH + 1 M NaBH <sub>4</sub>	2 M H <sub>2</sub> O <sub>2</sub> + 0.5 M H <sub>2</sub> SO <sub>4</sub>	37.4	25	[52]
Au/C	Pt/C	25% NaBH <sub>4</sub> + 6 M NaOH	1 M H <sub>2</sub> O <sub>2</sub> + 1 M HCl + 3 M NaCl	34	20	[53]
Au/C	Pt/C	1 M NaBH <sub>4</sub> + 3 M NaOH	$0.15\mathrm{MH_2O_2} + 1\mathrm{MHCl}$	25	25	[54]
Au-NP@rGO foam	Pd/C	0.4 M NaBH <sub>4</sub> + 2 M NaOH	$0.8 \mathrm{M}\mathrm{H}_2\mathrm{O}_2 + 2 \mathrm{M}\mathrm{H}_2\mathrm{SO}_4$	60	30	[55]
CoNi-NS/Ni foam	Pd/Ti	0.5 M NaBH <sub>4</sub> + 4 M NaOH	$0.8 \mathrm{M}\mathrm{H}_2\mathrm{O}_2 + 2 \mathrm{M}\mathrm{H}_2\mathrm{SO}_4$	80.6 140	30 60	[56]
Co <sub>4</sub> -Au <sub>1</sub> /C	Pt mesh	0.1 M NaBH <sub>4</sub> + 2 M NaOH	4.5 M H <sub>2</sub> O <sub>2</sub> + 2 M HCl	102.4	25	[57]
Ni-P@NF	Pt sheet	3 M NaOH + 1 M NaBH <sub>4</sub>	$0.5 \mathrm{M}\mathrm{H_2SO_4} + 2 \mathrm{M}\mathrm{H_2O_2}$	52.5	25	[58]
AuPPy-C	Pt mesh	2 M NaOH + 0.03 M NaBH <sub>4</sub>	1.5 M HCl + 5 M H <sub>2</sub> O <sub>2</sub>	74.6	25	[59]
Au/CNT-G	Pt/C	2 M NaBH <sub>4</sub> + 6 M NaOH	2 M H <sub>2</sub> O <sub>2</sub> + 1 M HCl	125	50	[60]
Au/MWCNTs	Au/MWCNTs	5 wt% NaBH <sub>4</sub> + 10 wt% NaOH + 85 wt% H <sub>2</sub> O	$20 \text{ wt\% } \text{H}_2\text{O}_2 + 5 \text{ wt\% } \text{H}_3\text{PO}_4 + \\ 75 \text{ wt\% } \text{H}_2\text{O}$	74	-	[61]

It was found that the DBHPFC using AuNPs-NiFe had a power density of 89.7 mW cm $^{-2}$  at 25 °C, which is significantly higher than that of Ni<sub>1</sub>@Au<sub>1</sub>/C (74.0 mW cm $^{-2}$ ) [16], Au<sub>50</sub>Fe<sub>50</sub>/C (34.9 mW cm $^{-2}$  at 25 °C) [46], Au<sub>58</sub>Ni<sub>42</sub>/C (45.74 mW cm $^{-2}$  at 20 °C) [49], Au/C (25.8 mW cm $^{-2}$ ) [50], Au@Co-B (85 mW cm $^{-2}$  at 25 °C) [51], Au-NP@rGO foam (60 mW cm $^{-2}$  at 30 °C) [55], AuPPy-C (74.6 mW cm $^{-2}$  at 25 °C) [59], and Au/MWCNTs C (74 mW cm $^{-2}$  at 25 °C) [61]. This enhanced performance is attributed to the synergistic interaction between the highly active AuNPs and the conductive NiFe matrix, which promotes efficient borohydride oxidation and electron transfer collectively. When integrated with NiFe, AuNPs introduce synergistic effects that can improve reaction kinetics, stability, and surface reactivity.

## 4. Conclusions

In this study, NiFe coatings were successfully synthesized via electroless deposition on a Cu/PI surface. The coatings were then modified with AuNPs through galvanic displacement to enhance their electrocatalytic performance in NaBH<sub>4</sub> electrooxidation. Scanning electron microscopy (SEM), energy-dispersive X-ray spectroscopy (EDX), X-ray diffraction (XRD), and inductively coupled plasma optical emission spectroscopy (ICP-OES) were used to examine the structural and morphological characteristics of the coatings, confirming the formation of a NiFe alloy matrix and the presence of dispersed AuNPs. Electrochemical characterization, including cyclic voltammetry, demonstrated that the AuNPs-modified NiFe coatings exhibited significantly enhanced catalytic performance, characterized by higher current densities, lower onset potentials, and reduced charge transfer resistance, compared to the unmodified NiFe coating. Further evaluation in a DBHPFCs configuration revealed that the AuNPs-NiFe anode exhibited a superior power density of 89.7 mW cm<sup>-2</sup> at room temperature and demonstrated operational stability under alkaline conditions, whereas the NiFe anode exhibited a power density of 73.1 mW cm<sup>-2</sup>. This enhanced performance is attributed to the synergistic interaction between the highly active AuNPs and the conductive NiFe matrix, which promotes efficient borohydride oxidation and electron transfer collectively. This work presents a novel, cost-effective, and highly active anode engineering strategy for DBHPFCs with a focus on NiFe-based materials modified with a noble metal for use in electrocatalytic NaBH<sub>4</sub> electrooxidation and other hydrogen-based energy systems.

Crystals 2025, 15, 819 13 of 16

**Author Contributions:** Conceptualization, L.T.-T. and H.A.; methodology, A.B., J.V., D.S. and B.Š.-S.; validation, E.N., A.B. and B.Š.-S.; formal analysis, A.Z., A.N. and A.B.; investigation, A.Z., A.N., J.V., D.S. and Z.M.; data curation, E.N. and J.V.; writing—original draft preparation, H.A. and L.T.-T.; writing—review and editing, E.N.; visualization, H.A., A.Z. and A.B.; supervision, L.T.-T.; project administration, L.T.-T.; funding acquisition, L.T.-T. All authors have read and agreed to the published version of the manuscript.

**Funding:** This research was funded by a grant (No. P-MIP-23-467) from the Research Council of Lithuania (LMTLT).

**Data Availability Statement:** The original contributions presented in this study are included in the article. Further inquiries can be directed to the corresponding authors.

**Acknowledgments:** The authors are grateful to Ramūnas Levinas from the Department of Catalysis, Center for Physical Sciences and Technology for materials characterization by XRD.

Conflicts of Interest: The authors declare no conflicts of interest.

# **Abbreviations**

The following abbreviations are used in this manuscript:

AuNPs Gold nanoparticles

BOR Sodium Borohydride Oxidation Reaction

CV Cyclic Voltammetry
CA Chronoamperometry
CP Chronopotentiometry
Cu/PI Copper-coated polyimide
DBFCs Direct Borohydride Fuel Cells

EDX Energy-Dispersive X-ray Spectroscopy

ICP-OES Inductively Coupled Plasma Optical Emission Spectroscopy

LSV Linear Sweep Voltammetry

MB Morpholine borane NaBH<sub>4</sub> Sodium Borohydride

NaBH<sub>4</sub>-H<sub>2</sub>O<sub>2</sub> Sodium Borohydride–Hydrogen Peroxide Fuel Cell

PI Polyimide

ORR Oxygen Reduction Reaction
SEM Scanning Electron Microscopy

SILAR Successive Ionic Layer Adsorption and Reaction

# References

- 1. Wang, J.; Ma, X.; Liu, T.; Liu, D.; Hao, S.; Du, G.; Kong, R.; Asiri, A.M.; Sun, X. NiS<sub>2</sub> nanosheet array: A high-active bifunctional electrocatalyst for hydrazine oxidation and water reduction toward energy-efficient hydrogen production. *Mater. Today Energy* **2017**, *3*, 9–14. [CrossRef]
- 2. Moradi, R.; Groth, K.M. Hydrogen storage and delivery: Review of the state-of-the-art technologies and risk and reliability analysis. *Int. J. Hydrogen Energy* **2019**, *44*, 12254–12269. [CrossRef]
- 3. He, B.; Zhuang, S.; Tai, X.; Zhang, J.; Xie, A.; Cheng, L.; Song, P.; Tang, Y.; Chen, Y.; Wan, P. Carbon coated and nitrogen doped hierarchical NiMo-based electrocatalysts with high activity and durability for efficient borohydride oxidation. *ACS Appl. Mater. Interfaces* **2022**, *14*, 17631–17641. [CrossRef] [PubMed]
- 4. Ma, J.; Choudhury, N.A.; Sahai, Y. A comprehensive review of direct borohydride fuel cells. *Renew. Sustain. Energy Rev.* **2010**, 14, 183–199. [CrossRef]
- 5. Yin, X.; Wang, Q.; Duan, D.; Liu, S.; Wang, Y. Amorphous NiB alloy decorated by Cu as the anode catalyst for a direct borohydride fuel cell. *Int. J. Hydrogen Energy* **2019**, *44*, 10971–10981. [CrossRef]
- 6. Braesch, G.; Wang, Z.; Sankarasubramanian, S.; Oshchepkov, A.G.; Bonnefont, A.; Savinova, E.R.; Ramani, V.; Chatenet, M. A high-performance direct borohydride fuel cell using bipolar interfaces and noble metal-free Ni-based anodes. *J. Mater. Chem. A* 2020, *8*, 20543–20552. [CrossRef]

7. Oshchepkov, A.G.; Braesch, G.; Ould-Amara, S.; Rostamikia, G.; Maranzana, G.; Bonnefont, A.; Papaefthimiou, V.; Janik, M.J.; Chatenet, M.; Savinova, E.R. Nickel metal nanoparticles as anode electrocatalysts for highly efficient direct borohydride fuel cells. *ACS Catal.* **2019**, *9*, 8520–8528. [CrossRef]

- 8. Xue, L.; Liu, C.; Ye, J.; Zhang, J.; Kang, L.; Zhang, Y.; Shi, W.; Guo, W.; Huang, X.; Yang, X.; et al. Engineering partially oxidized gold via oleylamine modifier as a high-performance anode catalyst in a direct borohydride fuel cell. *ACS Appl. Mater. Interfaces* **2024**, *16*, 39295–39304. [CrossRef]
- 9. Zhiani, M.; Mohammadi, I. Performance study of passive and active direct borohydride fuel cell employing a commercial Pd decorated Ni–Co/C anode catalyst. *Fuel* **2016**, *166*, 517–525. [CrossRef]
- 10. Santos, D.M.F.; Šljukić, B.; Amaral, L.; Milikić, J.; Sequeira, C.A.C.; Macciò, D.; Saccone, A. Nickel–rare earth electrodes for sodium borohydride electrooxidation. *Electrochim. Acta* **2016**, *190*, 1050–1056. [CrossRef]
- 11. Li, Y.; Zhang, X.; Zhang, Q.; Zheng, J.; Zhang, N.; Chen, B.H.; Smith, K.J. Activity and kinetics of ruthenium supported catalysts for sodium borohydride hydrolysis to hydrogen. *RSC Adv.* **2016**, *6*, 29371–29377. [CrossRef]
- 12. Cheng, K.; Jiang, J.; Kong, S.; Gao, Y.; Ye, K.; Wang, G.; Zhang, W.; Cao, D. Pd nanoparticles support on rGO-C@TiC coaxial nanowires as a novel 3D electrode for NaBH<sub>4</sub> electrooxidation. *Int. J. Hydrogen Energy* **2017**, *42*, 2943–2951. [CrossRef]
- 13. Yang, F.; Cheng, K.; Ye, K.; Wei, X.; Xiao, X.; Guo, F.; Wang, G.; Cao, D. High performance of Au nanothorns supported on Ni foam substrate as the catalyst for NaBH<sub>4</sub> electrooxidation. *Electrochim. Acta* **2014**, *115*, 311–316. [CrossRef]
- 14. Song, C.; Zhang, D.; Wang, B.; Cai, Z.; Yan, P.; Sun, Y.; Ye, K.; Cao, D.; Cheng, K.; Wang, G. Uniformly grown PtCo-modified Co<sub>3</sub>O<sub>4</sub> nanosheets as a highly efficient catalyst for sodium borohydride electrooxidation. *Nano Res.* **2016**, *9*, 3322–3333. [CrossRef]
- 15. Yi, L.; Meng, Y.; Wang, R.; Fei, J.; Wang, X.; Lu, Y. Carbon supported Pd–Sn nanoparticle eletrocatalysts for efficient borohydride electrooxidation. *New J. Chem.* **2020**, *44*, 13472–13479. [CrossRef]
- 16. Duan, D.; Liang, J.; Liu, H.; You, X.; Wei, H.; Wei, G.; Liu, S. The effective carbon supported core–shell structure of Ni@Au catalysts for electro-oxidation of borohydride. *Int. J. Hydrogen Energy* **2015**, *40*, 488–500. [CrossRef]
- 17. Duan, D.; Liu, H.; You, X.; Wei, H.; Liu, S. Anodic behavior of carbon supported Cu@Ag core–shell nanocatalysts in direct borohydride fuel cells. *J. Power Sources* **2015**, 293, 292–300. [CrossRef]
- 18. Duan, D.; Liu, H.; Wang, Q.; Wang, Y.; Liu, S. Kinetics of sodium borohydride direct oxidation on carbon supported Cu-Ag bimetallic nanocatalysts. *Electrochim. Acta* **2016**, *198*, 212–219. [CrossRef]
- 19. Balčiūnaitė, A.; Tamašauskaitė-Tamašiūnaitė, L.; Santos, D.M.F.; Zabielaitė, A.; Jagminienė, A.; Stankevičienė, I.; Norkus, E. Au nanoparticles modified Co/titania nanotubes as electrocatalysts for borohydride oxidation. *Fuel Cells* **2017**, *17*, 690–697. [CrossRef]
- 20. Zabielaitė, A.; Šimkūnaitė, D.; Balčiūnaitė, A.; Šimkūnaitė-Stanynienė, B.; Stalnionienė, I.; Naruškevičius, L.; Upskuvienė, D.; Selskis, A.; Tamašauskaitė-Tamašiūnaitė, L.; Norkus, E. Investigation of stability of gold nanoparticles modified zinc–cobalt coating in an alkaline sodium borohydride solution. *Chemija* 2020, 31, 210–223. [CrossRef]
- 21. Tiwari, A.; Singh, V.; Nagaiah, T.C. Non-noble cobalt tungstate catalyst for effective electrocatalytic oxidation of borohydride. *ACS Appl. Mater. Interfaces* **2019**, *11*, 21465–21472. [CrossRef]
- 22. Zhang, D.; Cheng, K.; Shi, N.; Guo, F.; Wang, G.; Cao, D. Nickel particles supported on multi-walled carbon nanotubes modified sponge for sodium borohydride electrooxidation. *Electrochem. Commun.* **2013**, *35*, 128–130. [CrossRef]
- 23. Oshchepkov, A.G.; Braesch, G.; Rostamikia, G.; Bonnefont, A.; Janik, M.J.; Chatenet, M.; Savinova, E.R. Insights into the borohydride electrooxidation reaction on metallic nickel from operando FTIRS, on-line DEMS and DFT. *Electrochim. Acta* 2021, 389, 138721. [CrossRef]
- 24. Çelikkan, H.; Şahin, M.; Aksu, M.L.; Veziroğlu, T.N. The investigation of the electrooxidation of sodium borohydride on various metal electrodes in aqueous basic solutions. *Int. J. Hydrogen Energy* **2007**, *32*, 588–593. [CrossRef]
- 25. Tamasauskaite-Tamasiunaite, L.; Lichusina, S.; Balciunaite, A.; Zabielaite, A.; Simkunaite, D.; Vaiciuniene, J.; Selskis, A.; Norkus, E. Zinc-cobalt alloy deposited on the titanium surface as electrocatalysts for borohydride oxidation. ECS Trans. 2014, 61, 49. [CrossRef]
- Braesch, G.; Oshchepkov, A.; Bonnefont, A.; Maranzana, G.; Rostamikia, G.; Janik, M.J.; Savinova, E.; Chatenet, M. Electrodeposited Ni-based electrodes for high-performance borohydride oxidation reaction. *Meet. Abstr.* 2021, MA2021-01, 1916. [CrossRef]
- 27. Santos, D.M.F.; Sequeira, C.A.C. Zinc anode for direct borohydride fuel cells. J. Electrochem. Soc. 2009, 157, B13. [CrossRef]
- 28. Geng, X.; Zhang, H.; Ye, W.; Ma, Y.; Zhong, H. Ni–Pt/C as anode electrocatalyst for a direct borohydride fuel cell. *J. Power Sources* **2008**, *185*, 627–632. [CrossRef]
- 29. Duan, D.; You, X.; Liang, J.; Liu, S.; Wang, Y. Carbon supported Cu-Pd nanoparticles as anode catalyst for direct borohydride-hydrogen peroxide fuel cells. *Electrochim. Acta* **2015**, *176*, 1126–1135. [CrossRef]
- 30. Venugopal, A.; Aluha, J.; Scurrell, M.S. The water-gas shift reaction over Au-based, bimetallic catalysts. The Au-M (M= Ag, Bi, Co, Cu, Mn, Ni, Pb, Ru, Sn, Tl) on Iron (III) oxide system. *Catal. Lett.* **2003**, *90*, 1–6. [CrossRef]

31. Naruškevičius, L.; Tamašauskaitė-Tamašiūnaitė, L.; Žielienė, A.; Jasulaitienė, V. A Co-based surface activator for electroless copper deposition. *Surf. Coat. Technol.* **2012**, 206, 2967–2971. [CrossRef]

- 32. Norkus, E.; Tamašauskaitė-Tamašiūnaitė, L. Application of Electroless Metal Deposition and Galvanic Displacement for Fabrication of Catalysts for Borohydride Oxidation. In *Encyclopedia of Interfacial Chemistry: Surface Science and Electrochemistry*; Wandelt, K., Ed.; Elsevier: Amsterdam, The Netherlands, 2018; Volume 5, pp. 361–372. [CrossRef]
- 33. Jing, P.; Liu, M.; Pu, Y.; Cui, Y.; Wang, Z.; Wang, J.; Liu, Q. Dependence of phase configurations, microstructures and magnetic properties of iron-nickel (Fe-Ni) alloy nanoribbons on deoxidization temperature in hydrogen. *Sci. Rep.* **2016**, *6*, 37701. [CrossRef] [PubMed]
- 34. Gyenge, E. Electrooxidation of borohydride on platinum and gold electrodes: Implications for direct borohydride fuel cells. *Electrochim. Acta* **2004**, *49*, 965–978. [CrossRef]
- 35. Liu, B.H.; Li, Z.P.; Suda, S. Anodic oxidation of alkali borohydrides catalyzed by nickel. *J. Electrochem. Soc.* **2003**, *150*, A398–A402. [CrossRef]
- 36. Hosseini, M.G.; Abdolmaleki, M.; Ashrafpoo, S. Electrocatalytic oxidation of sodium borohydride on a nanoporous Ni/Zn-Ni electrode. *Chin. J. Catal.* **2012**, *33*, 1817–1824. [CrossRef]
- 37. Robertson, P.M. On the oxidation of alcohols and amines at nickel oxide electrodes: Mechanistic aspects. *J. Electroanal. Chem. Interf. Electrochem.* **1980**, 111, 97–104. [CrossRef]
- 38. Aytaç, A.; Gürbüz, M.; Elif Sanli, A. Electrooxidation of hydrogen peroxide and sodium borohydride on Ni deposited carbon fiber electrode for alkaline fuel cells. *Int. J. Hydrogen Energy* **2011**, *36*, 10013–10021. [CrossRef]
- 39. Zhang, C.; Park, S.M. The anodic oxidation of nickel in alkaline media studied by spectroelectrochemical techniques. *J. Electrochem. Soc.* **1987**, 134, 2966–2970. [CrossRef]
- 40. Kuczyński, M.; Mikołajczyk, T.; Pieroźyński, B. Alkaline water splitting by Ni-Fe nanoparticles deposited on carbon fibre and nickel-coated carbon fibre substrates. *Catalysts* **2023**, *13*, 1468. [CrossRef]
- 41. Wehrens-Dijksma, M.; Notten, P.H.L. Electrochemical quartz microbalance characterization of Ni(OH)<sub>2</sub>-based thin film electrodes. *Electrochim. Acta* **2006**, *51*, 3609–3621. [CrossRef]
- 42. He, P.; Wang, X.; Liu, Y.; Liu, X.; Yi, L. Comparison of electrocatalytic activity of carbon-supported Au–M (M = Fe, Co, Ni, Cu and Zn) bimetallic nanoparticles for direct borohydride fuel cells. *Int. J. Hydrogen Energy* **2012**, *37*, 11984–11993. [CrossRef]
- 43. Arevalo, R.L.; Escano, M.C.S.; Wang, A.Y.-S.; Kasai, H. Structure and stability of borohydride on Au(111) and Au3M(111) (M = Cr, Mn, Fe, Co, Ni) surfaces. *Dalt. Trans.* **2013**, 42, 770–775. [CrossRef]
- 44. Finkelstein, D.A.; Letcher, C.D.; Jones, D.J.; Sandberg, L.M.; Watts, D.J.; Abruña, H.D. Self-poisoning during BH<sub>4</sub><sup>-</sup> oxidation at Pt and Au, and in situ poison removal procedures for BH<sub>4</sub><sup>-</sup> fuel cells. *J. Phys. Chem C* **2013**, *117*, 1571–1581. [CrossRef]
- 45. Nagle, L.C.; Rohan, J.F. Nanoporous gold anode catalyst for direct borohydride fuel cell. *Int. J. Hydrogen Energy* **2011**, *36*, 10319–10326. [CrossRef]
- 46. Duan, D.; Yin, X.; Wang, Q.; Liu, S.; Wang, Y. Performance evaluation of borohydride electrooxidation reaction with ternary alloy Au–Ni–Cu/C catalysts. *J. Appl. Electrochem.* **2018**, *48*, 835–847. [CrossRef]
- 47. Backović, G.; Milikić, J.; Negric, S.D.; Saccone, A.; Šljukić, B.; Santos, D.M.F. Enhanced borohydride oxidation kinetics at gold-rare earth alloys. *J. Alloys Compn.* **2021**, *857*, 158273. [CrossRef]
- 48. Yi, L.; Wei, W.; Zhao, C.; Tian, L.; Liu, J.; Wang, X. Enhanced activity of Au–Fe/C anodic electrocatalyst for direct borohydride-hydrogen peroxide fuel cell. *J. Power Sources* **2015**, *285*, 325–333. [CrossRef]
- 49. He, P.; Wang, Y.; Wang, X.; Pei, F.; Wang, H.; Liu, L.; Yi, L. Investigation of carbon supported Au–Ni bimetallic nanoparticles as electrocatalyst for direct borohydride fuel cell. *J. Power Sources* **2011**, *196*, 1042–1047. [CrossRef]
- 50. Wei, J.L.; Wang, X.Y.; Wang, Y.; Guo, J.; He, P.Y.; Yang, S.; Li, N.; Pei, F.; Wang, Y.S. Carbon-supported Au hollow nanospheres as anode catalysts for direct borohydride—hydrogen peroxide fuel cells. *Energy Fuels* **2009**, 23, 4037–4041. [CrossRef]
- 51. Li, S.; Wang, L.; Chu, J.; Zhu, H.; Chen, Y.; Liu, Y. Investigation of Au@Co-B nanoparticles as anode catalyst for direct borohydride fuel cells. *Int. J. Hydrogen Energy* **2016**, *41*, 8583–8588. [CrossRef]
- 52. Yi, L.; Song, Y.; Liu, X.; Wang, X.; Zou, G.; He, P.; Yi, W. High activity of Au–Cu/C electrocatalyst as anodic catalyst for direct borohydride-hydrogen peroxide fuel cell. *Int. J. Hydrogen Energy* **2011**, *36*, 15775–15782.
- 53. Ponce de León, C.; Walsh, F.C.; Rose, A.; Lakeman, J.B.; Browning, D.J.; Reeve, R.W. A direct borohydride—Acid peroxide fuel cell. *J. Power Sources* **2007**, *164*, 441–448. [CrossRef]
- 54. Atwan, M.H.; Macdonald, C.L.; Northwood, D.O.; Gyenge, E.L. Colloidal Au and Au-alloy catalysts for direct borohydride fuel cells: Electrocatalysis and fuel cell performance. *J. Power Sources* **2006**, *158*, 36–44. [CrossRef]
- 55. Li, B.; Song, C.; Huang, X.; Ye, K.; Cheng, K.; Zhu, K.; Yan, J.; Cao, D.; Wang, G. A novel anode for direct borohydride-hydrogen peroxide fuel cell: Au nanoparticles decorated 3D self-supported reduced graphene oxide foam. *ACS Sustain. Chem. Eng.* **2019**, 7, 11129–11137. [CrossRef]

56. Li, B.; Yan, Q.; Song, C.; Yan, P.; Ye, K.; Cheng, K.; Zhu, K.; Yan, J.; Cao, D.; Wang, G. Reduced graphene oxide foam supported CoNi nanosheets as an efficient anode catalyst for direct borohydride hydrogen peroxide fuel cell. *Appl. Surf. Sci.* **2019**, 491, 659–669. [CrossRef]

- 57. Duan, D.; Feng, J.; You, X.; Zhou, X.; Wang, Y.; Chen, L.; Liu, S. Evaluation of Co–Au bimetallic nanoparticles as anode electrocatalyst for direct borohydride-hydrogen peroxide fuel cell. *Ionics* **2021**, 27, 3521–3532.
- 58. Yu, J.; Hu, B.; Xu, C.; Meng, J.; Yang, S.; Li, Y.; Zhou, X.; Liu, Y.; Yu, D.; Chen, C. An efficient Ni–P amorphous alloy electrocatalyst with a hierarchical structure toward borohydride oxidation. *Dalton Trans.* **2021**, *50*, 10168–10179. [CrossRef]
- 59. Milikić, J.; Tapia, A.; Stamenović, U.; Vodnik, V.; Otoničar, M.; Škapin, S.; Santos, D.M.; Šljukić, B. High-performance metal (Au, Cu)–polypyrrole nanocomposites for electrochemical borohydride oxidation in fuel cell applications. *Int. J. Hydrogen Energy* **2022**, 47, 36990–37001. [CrossRef]
- 60. Uzundurukan, A.; Akça, E.S.; Budak, Y.; Devrim, Y. Carbon nanotube-graphene supported bimetallic electrocatalyst for direct borohydride hydrogen peroxide fuel cells. *Renew. Energy* **2021**, *172*, 1351–1364. [CrossRef]
- 61. Oh, T.H. Gold-based bimetallic electrocatalysts supported on multiwalled carbon nanotubes for direct borohydride–hydrogen peroxide fuel cell. *Renew. Energy* **2021**, *163*, 930–938.

**Disclaimer/Publisher's Note:** The statements, opinions and data contained in all publications are solely those of the individual author(s) and contributor(s) and not of MDPI and/or the editor(s). MDPI and/or the editor(s) disclaim responsibility for any injury to people or property resulting from any ideas, methods, instructions or products referred to in the content.